Electronic structure examination of the topological properties of $CaMnSb_2$ by angle-resolved photoemission spectroscopy

Hongtao Rong,[1,2] Liqin Zhou,[1,2] Junbao He,[1,2,3] Chunyao Song,[1,2] Jianwei Huang,[1,2] Cheng Hu,[1,2] Yu Xu,[1,2] Yongqing Cai,[1,2] Hao Chen,[1,2] Cong Li,[1,2] Qingyan Wang,[1,2] Lin Zhao,[1,2,4] Zhihai Zhu,[1,2] Guodong Liu,[1,2,4] Zuyan Xu,[5] Genfu Chen,[1,2] Hongming Weng,[1,2] and X. J. Zhou[1,2,4,6,*]

[1]*National Lab for Superconductivity, Beijing National Laboratory for Condensed Matter Physics, Institute of Physics, Chinese Academy of Sciences, Beijing 100190, China*

[2]*University of Chinese Academy of Sciences, Beijing 100049, China*

[3]*Henan International Joint Laboratory of MXene Materials Microstructure, College of Physics and Electronic Engineering, Nanyang Normal University, Nanyang 473061, China*

[4]*Songshan Lake Materials Laboratory, Dongguan 523808, China*

[5]*Technical Institute of Physics and Chemistry, Chinese Academy of Sciences, Beijing 100190, China*

[6]*Beijing Academy of Quantum Information Sciences, Beijing 100193, China*

(Received 9 March 2021; accepted 12 May 2021; published 1 June 2021)

We have carried out detailed high-resolution angle-resolved photoemission spectroscopy measurements and band structure calculations to study the electronic structure of $CaMnSb_2$. The observed Fermi surface mainly consists of one hole pocket around the Γ point and one tiny hole pocket at the Y point. Strong spectral weight accumulation along the Γ-X direction is observed on the holelike Fermi surface around the Γ point, suggesting strong anisotropy of the density of states along the Fermi surface. The tiny hole pocket at the Y point originates from an anisotropic Dirac-like band with the crossing point of the linear bands lying ∼10 meV above the Fermi level. These observations are in good agreement with the band structure calculations. In addition, we observe additional features along the Γ-Y line that cannot be accounted for by the band structure calculations. Our results provide important information in the understanding and exploration of novel properties in $CaMnSb_2$ and related materials.

DOI: 10.1103/PhysRevB.103.245104

I. INTRODUCTION

Topological materials have attracted much attention due to their novel quantum phenomena and physical properties as well as potential applications [1–7]. Various types of topological materials have been discovered, including quantum spin Hall states [8–11], three-dimensional topological insulators [12–17], Dirac semimetals [18–24], Weyl semimetals [25–30], and topological node-line semimetals [4,31–34]. The Dirac materials present peculiar behaviors due to the presence of Dirac fermions. In Dirac materials, the low-energy excitations have a relativistic nature, and these quasiparticles obey Dirac equations, instead of the conventional Schrödinger equation [6]. These Dirac fermions may give rise to exotic transport properties [35–37], such as the anomalous quantum Hall effect [38,39], the chiral anomaly [40,41], ultrahigh mobility, giant magnetoresistance [42–45], and Aharonov-Bohm oscillations [46].

$AMnP_2$ (A=Ca, Sr, Ba, Eu, or Yb; P=Sb or Bi) compounds have become a fertile playground for exploration of topological materials [47–59]. $AMnP_2$ materials feature a common layered structure with an alternative stacking of A-P-A layers and MnP_4 layers, as exemplified by $CaMnSb_2$ in Fig. 1(a). In the A-P-A layer, the basic building block is the P sheet (P=Sb or Bi) in a regular or distorted square lattice, which can form highly anisotropic Dirac cones [47,50,60] or Weyl cones [56]. In the MnP_4 layers that are expected to be less conducting, Mn atoms are located at the center of edge-sharing tetrahedrons, and the magnetic moments of the Mn atoms are ordered antiferromagnetically below the Néel temperature near room temperature. Dirac fermions in $AMnP_2$ have been found to interplay with magnetism, leading to novel exotic properties, as demonstrated in $Sr_{1-y}Mn_{1-z}Sb_2$ ($y, z < 0.1$) [51], $EuMnBi_2$ [52], and $YbMnBi_2$ [56]. Compared with $AMnSb_2$, $AMnBi_2$ has stronger spin-orbit coupling (SOC) due to heavier Bi atoms that opens a larger gap at Dirac nodes, leading to massive Dirac fermions [47,50,60]. Replacement of Bi in $AMnP_2$ materials by lighter elements such as Sb is expected to reduce the gap to achieve massless Dirac fermions.

$CaMnSb_2$ crystalizes in the $Pnma$ space group [61]. Compared with the crystal structure of $AMnBi_2$, instead of forming a Bi square net plane, the Sb atoms in the Ca-Sb-Ca layer form zigzag chains [Fig. 1(b)]. The magnetotransport measurements suggest that $CaMnSb_2$ is a quasi-two-dimensional system that hosts nearly massless Dirac fermions [61]. However, the infrared spectroscopic measurements indicate that $CaMnSb_2$ is a topologically trivial insulator [62]. Angle-resolved photoemission spectroscopy (ARPES) is a powerful tool which can directly reveal the topological properties of $CaMnSb_2$, but so far no ARPES measurements have been reported for $CaMnSb_2$. In this paper, we carry out detailed

*Corresponding author: xjzhou@aphy.iphy.ac.cn

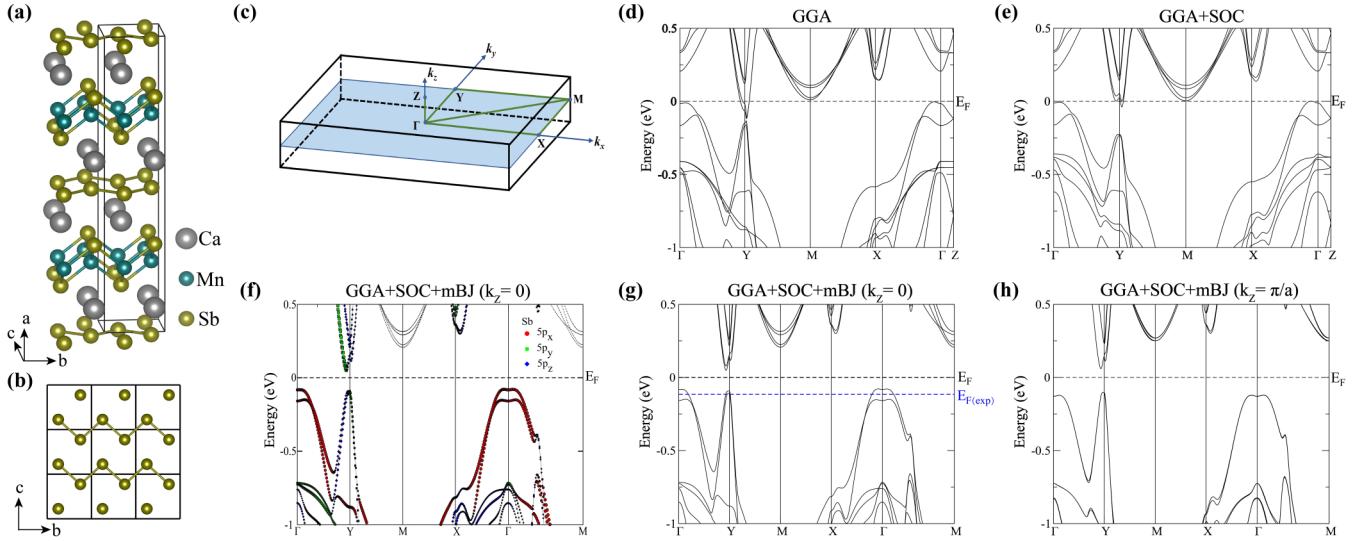

FIG. 1. Crystal structure and calculated band structures of $CaMnSb_2$. (a) Crystal structure of $CaMnSb_2$. The unit cell is indicated by black lines. It crystalizes in an orthorhombic structure (space group: *Pnma*) with lattice constants $a = 22.09$ Å, $b = 4.32$ Å, and $c = 4.35$ Å. (b) Top view of the central Sb layer, which consists of a zigzag chainlike structure along the b axis. (c) Three-dimensional Brillouin zone of $CaMnSb_2$. Green lines indicate high-symmetry directions. (d) and (e) Calculated band structure of $CaMnSb_2$ (d) without and (e) with spin-orbit coupling at $k_z = 0$. (f) Calculated band structure of $CaMnSb_2$ by considering spin-orbit coupling and the mBJ potential at $k_z = 0$. The bands near the Fermi level originate mainly from the Sb $5p_x$ (red circles), $5p_y$ (green squares), and $5p_z$ (blue diamonds) orbitals. Calculated band structure of $CaMnSb_2$ by considering spin-orbit coupling and mBJ potential at(g) $k_z = 0$ and (h) $k_z = \pi/a$.

high-resolution ARPES measurements and band structure calculations to study the electronic structure of $CaMnSb_2$. The observed Fermi surface mainly consists of one hole pocket around the Γ point and one tiny hole pocket at the Y point. The tiny hole pocket at the Y point originates from an anisotropic Dirac-like band that may play an important role in dictating the physical properties of $CaMnSb_2$.

II. EXPERIMENT

High-quality single crystals of $CaMnSb_2$ were grown by the flux method [61]. ARPES measurements were performed with our laboratory-ARPES system equipped with a 6.994 eV vacuum-ultraviolet (VUV) laser, 21.218 eV helium discharge lamp, and Scienta DA30L electron energy analyzer [63,64]. The energy resolutions for the VUV laser and helium discharge lamp ARPES measurements were set at ∼1 and 20 meV, respectively. The angular resolution was ∼0.3°. The Fermi level is referenced by measuring on the Fermi edge of clean polycrystalline gold that is electrically connected to the sample. All the samples were cleaved *in situ* and measured in ultrahigh vacuum with a base pressure better than 5×10^{-11} mbar.

The electronic structure calculation of $CaMnSb_2$ based on the density functional theory (DFT) were performed by using the Vienna Ab initio Simulation Package (VASP) [65]. The generalized gradient approximation of the Perdew-Burke-Ernzerhof type was selected to describe the exchange-correlation function [66], and the modified Becke-Johnson (mBJ) potential was used to achieve accurate band gap calculations [67,68]. The cutoff energy was set to 500 eV, and the Brillouin zone integration was sampled by a $3 \times 11 \times 11$ k mesh. SOC was taken into account. The tight-binding model of $CaMnSb_2$ was constructed with WANNIER90 with Sb $5p$ orbitals and Mn $3d$ orbitals, which are based on the maximally localized Wannier functions [69]. The bulk Fermi surfaces and projected surface states of $CaMnSb_2$ were calculated by the WANNIERTOOLS package [70].

III. RESULTS AND DISCUSSION

Figure 1 shows the crystal structure and the calculated band structures of $CaMnSb_2$. Figure 1(a) shows the crystal structure of $CaMnSb_2$, which consists of an alternate stacking of $MnSb_4$ layers and Ca-Sb-Ca layers along the a axis. In the Ca-Sb-Ca layer, the central Sb sheet is sandwiched in between two Ca layers; the Sb atoms in the Sb sheet form zigzag chains with the chain direction along the b axis [Fig. 1(b)]. It has a space group of *Pnma* and an orthorhombic crystal structure with lattice constants of $a = 22.09$ Å, $b = 4.32$ Å, and $c = 4.35$ Å. The corresponding Brillouin zone is shown in Fig. 1(c). Figure 1(d) shows the overall calculated band structure of $CaMnSb_2$ without considering SOC. The low-energy band structure near the Γ point mainly consists of two bands. The band structure near the Y point shows a Dirac-cone-like structure. However, even without considering SOC, a small gap already opens at the Dirac point, and the position of the Dirac point deviates slightly from the Y point along the Y-M direction. When SOC is taken into account, it has little effect on the bands near the Γ point but dramatically changes the band structure near the Y point. The gap at the Dirac point is greatly enhanced up to ∼180 meV. In the meantime, the band top of the lower branch shifts to the Y point along the Y-M direction. In order to get an accurate band gap, we carried out band structure calculations of $CaMnSb_2$ by using the mBJ potential [67,68], as shown in Figs. 1(g) and 1(h) for $k_z = 0$ and $k_z = \pi/a$, respectively. The inclusion of the mBJ potential alters the relative energy position of the bands near the Γ point

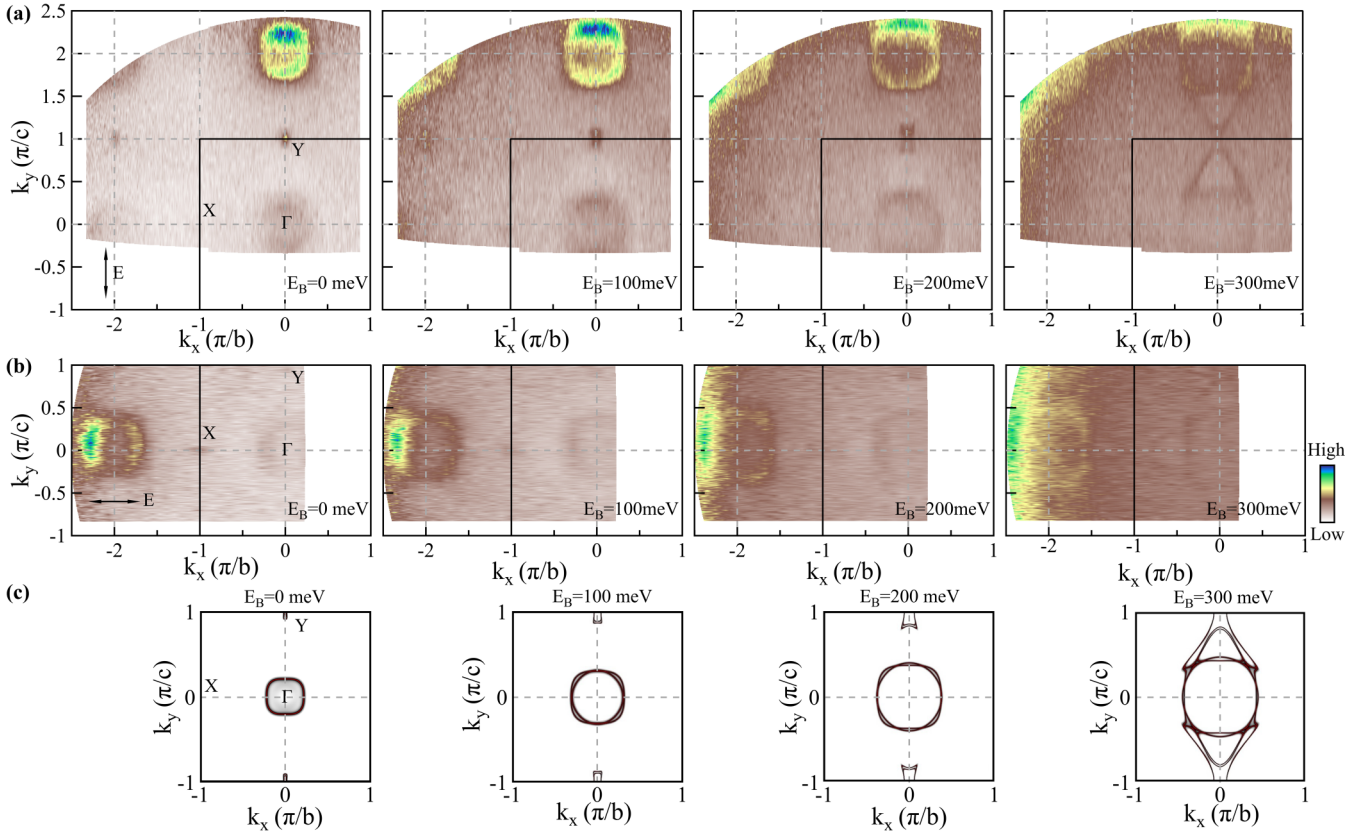

FIG. 2. Measured and calculated Fermi surface mapping and constant-energy contours of $CaMnSb_2$. (a) Constant-energy contours of $CaMnSb_2$ at binding energies of 0, 100, 200, and 300 meV measured at 30 K with a 21.218 eV helium lamp. The major E vector is along k_y direction, as marked by the arrow at the bottom-left inset of the left-most panel. (b) Same as (a). The major E vector is along the k_x direction, as marked by the arrow at the bottom left inset in the leftmost panel. All constant-energy contours in (a) and (b) are obtained by integrating the photoemission spectral weight over a [−20, 20] meV energy window with respect to the corresponding binding energy. The first Brillouin zone is indicated by the black squares. (c) Calculated constant-energy contours at binding energies of 0, 100, 200, and 300 meV for $k_z = 0$. An experimental Fermi level, $E_{F(exp)}$, is taken which is 0.12 eV below the Fermi level in the calculation, as shown in Fig. 1(g).

and the Y points. The initial bands at high binding energy are pushed further to even higher binding energy. It is interesting to note that the two main bands at the Γ point and the Y points for $k_z = 0$ [Fig. 1(g)] become nearly degenerate when k_z moves to π/a [Fig. 1(h)]. We also analyzed the orbital contributions to the low-energy bands, as shown in Fig. 1(f). The bands near the Fermi level originate mainly from the Sb $5p$ orbitals. Moreover, the bands near the Γ point mainly come from the Sb $5p_x$ orbitals, while the bands near the Y point along the Y-Γ and Y-M directions are mainly from Sb $5p_z$ and $5p_y$ orbitals, respectively.

Figure 2 shows the $CaMnSb_2$ Fermi surface and constant-energy contours at different binding energies measured using 21.218 eV photon energy. In order to obtain complete electronic structures, we carried out ARPES measurements under two distinct polarization geometries. When the electric vector of the light is along the Γ-Y direction [Fig. 2(a)], the observed Fermi surface consists mainly of a circular sheet around Γ and a strong spot at Y [leftmost panel in Fig. 2(a)]; no feature at X is observed. With increasing binding energy, the central circular sheet increases in area, indicating the corresponding Fermi surface is holelike. The area of the holelike pocket is estimated to be ∼0.1 $Å^{-2}$. In the meantime, the strong spot at Y also increases in area up to a binding energy of ∼200 meV; a trianglelike feature develops at higher binding energy, and it connects the Y point and the central circular sheet [rightmost panel in Fig. 2(a)]. When the electric vector of the light is switched to be along the Γ-X direction [Fig. 2(b)], a similar holelike Fermi surface is observed around Γ. However, in this case, the strong spot appears at X but is absent at Y.

The calculated Fermi surface and constant-energy contours of $CaMnSb_2$ [Fig. 2(c)] show good agreement with the measured results in Fig. 2(a). The zigzag Sb chains in $CaMnSb_2$ give rise to the highly anisotropic electronic structure that leads to the observation of a tiny pocket at Y but its absence at X. Since the bands near the Y point are mainly composed of Sb $5p_z$ and $5p_y$ orbitals [Fig. 1(f)], by considering the matrix element effects in the photoemission process, the states are allowed under the polarization geometry used [Fig. 2(a)]. The observation of the tiny pocket around the X point in Fig. 2(b) can be explained by the presence of two orthogonal domains in the orthorhombic bc plane of $CaMnSb_2$. The twin structure was revealed previously in the related sister compounds $SrMnSb_2$ [71] and $BaMnSb_2$ [59]. Our measured Fermi surface of $CaMnSb_2$ is also consistent with that of single-domain $SrMnSb_2$ [71].

Now we zoom in on the detailed electronic structure around the Y point in $CaMnSb_2$. Fig. 3(a) shows the

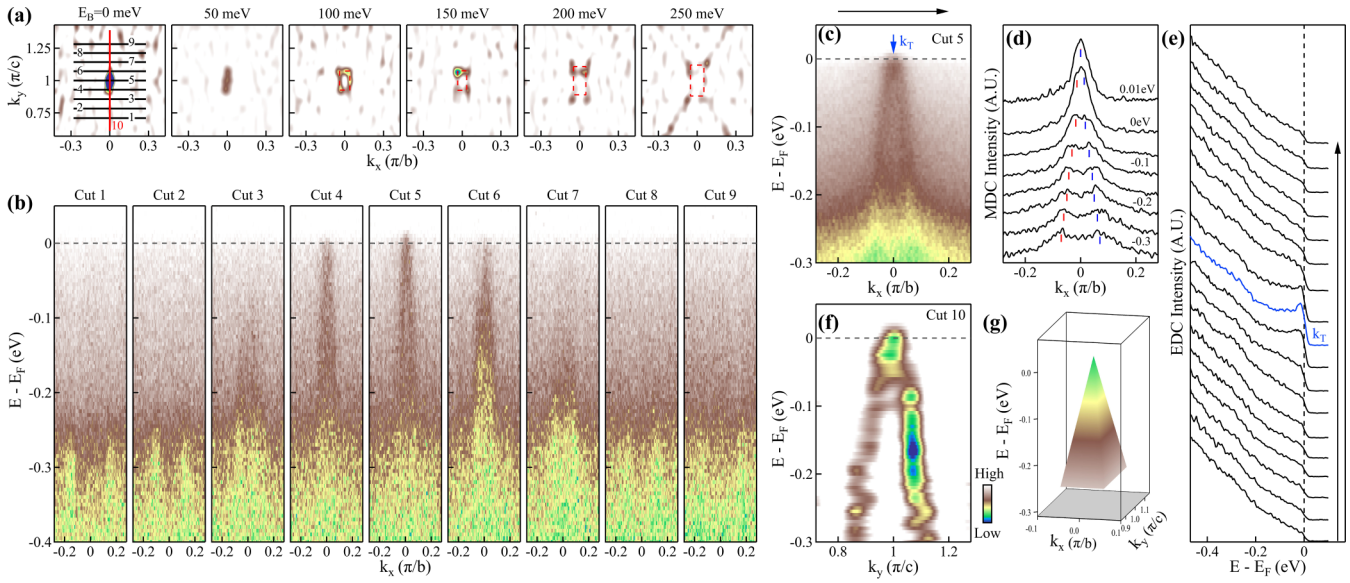

FIG. 3. Dirac-cone-like structure around the Y point in $CaMnSb_2$ measured with 21.218 eV photon energy at 30 K. (a) The second-derivative constant-energy contours around the Y point obtained by integrating the photoemission spectral weight over a [−20, 20] meV energy window with respect to binding energies of 0, 50, 100, 150, 200, and 250 meV. (b) Band structure measured along various momentum cuts. The locations of the momentum cuts, cut 1 to cut 9, are marked by black lines in the leftmost panel of (a). (c) Detailed band structure taken along momentum cut 5 that is along the YM direction crossing the Y point. (d) Momentum distribution curves (MDCs) of the photoemission image in (c) at different binding energies. (e) Photoemission spectra (energy dispersion curves, EDCs) at different momenta from photoemission image in (c). The blue line represents the EDC at the Y point [marked by the blue arrow and k_T in (c)]. (f) Band structure taken along momentum cut 10. The location of cut 10 is marked by the red line in the leftmost panel in (a) that crosses the Y point. The image is the second derivative of the original data with respect to the momentum. (g) Three-dimensional schematic of the Dirac-cone-like structure at the Y point.

constant-energy contours around the Y point at different binding energies. With increasing binding energy, the tiny hole pocket around the Y point gradually goes from an ellipselike to rectanglelike shape. Figure 3(b) shows the band evolution along the different momentum cuts around Y. Dirac-cone-like bands centered around Y (cut 5) are observed from cut 3 to cut 7 which contribute to the formation of the tiny hole pocket around the Y point. We also observe additional bands around $k_x = \pm 0.2$ (π/b) at a binding energy higher than 250 meV [cuts 1, 2, 8, and 9 in Fig. 3(b)]. These bands contribute to the trianglelike feature that connects the Y point and the central circular sheet in the constant energy contour [rightmost panel in Fig. 2(a)]. The Dirac-like band along cut 5 (the Y-M direction crossing the Y point) exhibits steep linear dispersion, as seen in Fig. 3(c). From the corresponding momentum distribution curves (MDCs) at different binding energies [Fig. 3(d)], we find that the two peaks in the MDCs at high binding energies gradually evolve into a single peak at ∼10 meV above the Fermi level. This indicates the crossing point of the two branches of the Dirac-like band lies around 10 meV above the Fermi level. The linear fitting of the MDC dispersions in Fig. 3(d) yields a Fermi velocity of ∼4.3 eV Å. Figure 3(e) shows the corresponding photoemission spectra (energy distribution curves, EDCs) of Fig. 3(c). A peak can be observed for the EDC at the Y point [k_T as marked in Fig. 3(c)]. The band structure along the Γ-Y direction crossing the Y point [cut 10 in Fig. 3(a)] is shown in Fig. 3(f). It also exhibits a Dirac-like band structure with a less steep dispersion than the one in Fig. 3(c), giving a Fermi velocity of ∼2.2 eV Å. Combining the results in Figs. 3(a), 3(c) and 3(f), we arrive at a three-dimensional pyramid that represents an anisotropic Dirac-cone-like structure in momentum space near the Y point.

Next, we investigate the detailed electronic structure of $CaMnSb_2$ around the Γ point. In addition to the measurements using the helium discharge lamp [$h\nu = 21.218$ eV; Fig. 2(a)], we also carried out high-resolution ARPES measurements using a laser ($h\nu = 6.994$ eV). Figures 4(a) and 4(b) show Fermi surface mappings measured under two different photon polarizations using the 6.994 eV laser. The holelike Fermi surface around Γ, seen in Figs. 2(a) and 2(b) with a 21.218 eV helium lamp, is more clearly observed using the 6.994 eV laser. The area of the holelike Fermi pocket around the Γ point in Figs. 4(a) and 4(b) is estimated to be about 0.17 $Å^{-2}$, which is slightly different from that measured by the helium lamp [∼0.1 $Å^{-2}$; Figs. 2(a) and 2(b)], reflecting the k_z dependence of the electronic structure. It is interesting to note that the spectral weight along the holelike Fermi surface in Figs. 4(a) and 4(b) exhibits a strong variation. Under the horizontal light polarization in Fig. 4(a), two strong spots are observed on the Fermi surface along the horizontal Γ-X direction while the spectral weight along the vertical Γ-Y direction is apparently suppressed. When the light polarization is switched to the vertical direction in Fig. 4(b), the two strong spots on the Fermi surface also change to the vertical Γ-Y direction while the spectral weight along the horizontal Γ-X direction is suppressed.

In order to understand the origin of the strong intensity variation along the Fermi surface [Figs. 4(a) and 4(b)], we present in Fig. 4(c) the band structures along different

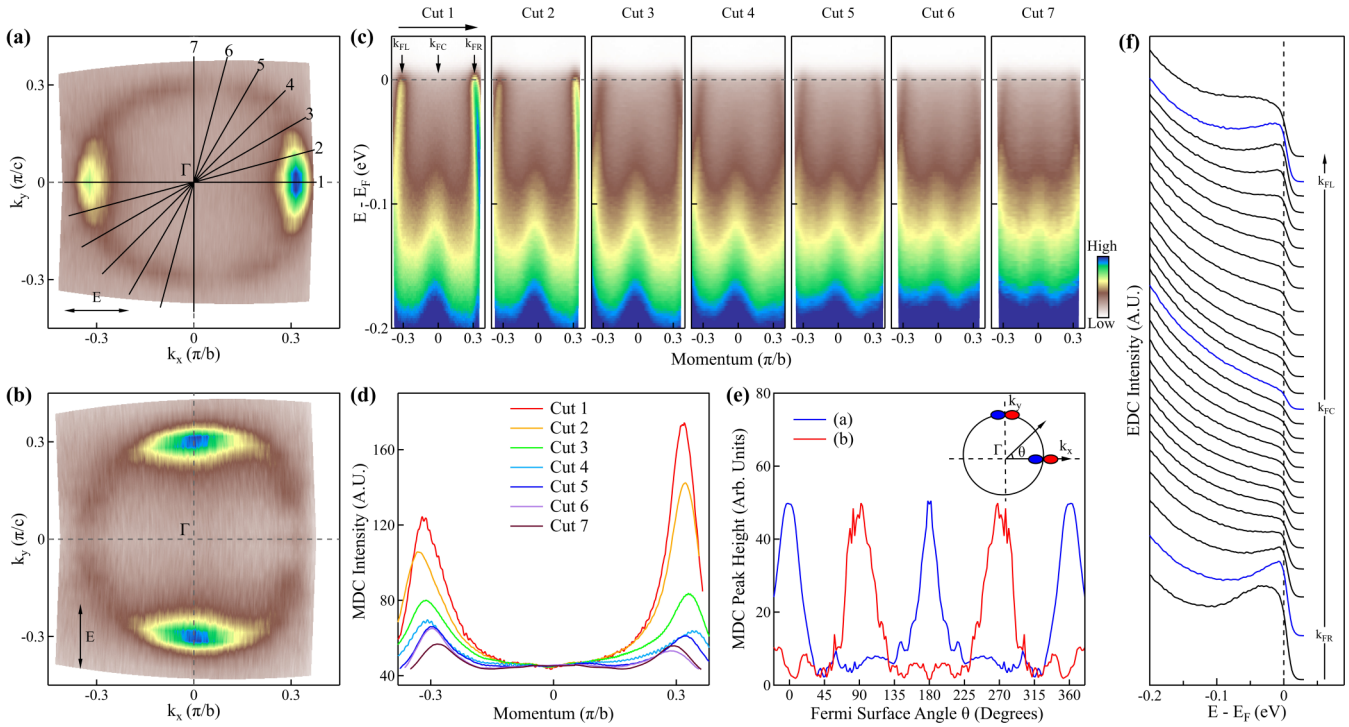

FIG. 4. Detailed holelike Fermi surface and band structures of $CaMnSb_2$ around the Γ point measured at 30 K. (a) Fermi surface mapping measured with a 6.994 eV laser by integrating the photoemission spectral weight over a [−10, 10] meV energy window. The E vector is along the k_x direction, as marked by the arrow in the bottom left corner. (b) Same as (a), but the E vector is along the k_y direction, as marked by the arrow in the bottom left corner. (c) Band structure measured along various momentum cuts; the locations of the momentum cuts are marked by black lines in (a). (d) MDCs at the Fermi level from the bands in (c) measured along various momentum cuts. (e) The angle-dependent MDC peak height along the Fermi surface in (a) (blue line) and (b) (red line) as a function of the Fermi surface angle. The Fermi surface angle θ is defined in the inset. The entire holelike Fermi pocket is composed of the Sb p_x orbital. (f) EDCs at different momenta from the cut 1 photoemission image [leftmost panel in (c)]. The EDCs at the Fermi momenta on the left side (k_{FL}) and right side (k_{FR}) of the band and at the Γ point (k_{FC}) are marked by blue lines.

momentum cuts crossing the Γ point from the data in Fig. 4(a). Figure 4(d) shows the MDCs at the Fermi level from the bands in Fig. 4(c). Indeed, the intensity of the holelike bands drops dramatically when the momentum cut changes from the horizontal Γ-X direction to the vertical Γ-Y direction, as seen directly from the band intensity in Fig. 4(c) and the MDC peak intensity in Fig. 4(d). Figure 4(e) shows quantitatively the spectral weight variation along the Fermi surface by plotting the MDC peak intensity as a function of the Fermi surface angle θ. When the light polarization E is horizontal [Fig. 4(a)], the spectral weight along the holelike Fermi surface peaks sharply at $\theta = 0^\circ$ and 180° [blue line in Fig. 4(e)]. When the light polarization E is vertical [Fig. 4(b)], the sharp spectral weight peak along the holelike Fermi surface changes to $\theta = 90^\circ$ and 270° [red line in Fig. 4(e)]. Figure 4(f) shows EDCs along the Γ-X momentum cut. The EDCs on the holelike Fermi surface near the strong spot region show broad peaks rather than sharp quasiparticle peaks, which indicates that the electronic states along the holelike Fermi surface experience strong scattering.

The first issue to address is whether the strong spot feature is a part of the holelike Fermi surface or is a new feature in addition to the holelike Fermi surface. Careful examination of the band structures near the strong spot region indicates that there is only a single holelike band; no indication of two coexisting features is observed [Fig. 4(c)]. This indicates that the strong spot feature is part of the holelike Fermi surface. The second issue concerns whether the strong spots originate from the photoemission matrix element effect. The band structure calculations have shown that the entire holelike Fermi surface is composed of Sb p_x orbitals, as schematically shown in the inset of Fig. 4(e). When the light polarization is horizontal, as in the case of Fig. 4(a), all the states along the holelike Fermi surface are allowed according to the matrix element effect analysis. If the density of states along the Fermi surface is uniform, one would expect to observe a uniform spectral weight distribution along the holelike Fermi surface that is not consistent with the observation of two strong spots on the Fermi surface. These results suggest that the density of states along the holelike Fermi surface is strongly anisotropic; there is a large accumulation of the density of states peaked along the Γ-X direction. Such confinement of a strong density of states at two particular points along the Fermi surface is unusual, and its effect on the physical properties is interesting to investigate. The polarization dependence of the measured Fermi surface mappings in Figs. 4(a) and 4(b) can be understood when the two coexisting kinds of domains (represented by domains A and B) are considered. For a given polarization in Fig. 4(a), from the photoemission matrix element effect analysis the electronic states along the entire holelike Fermi

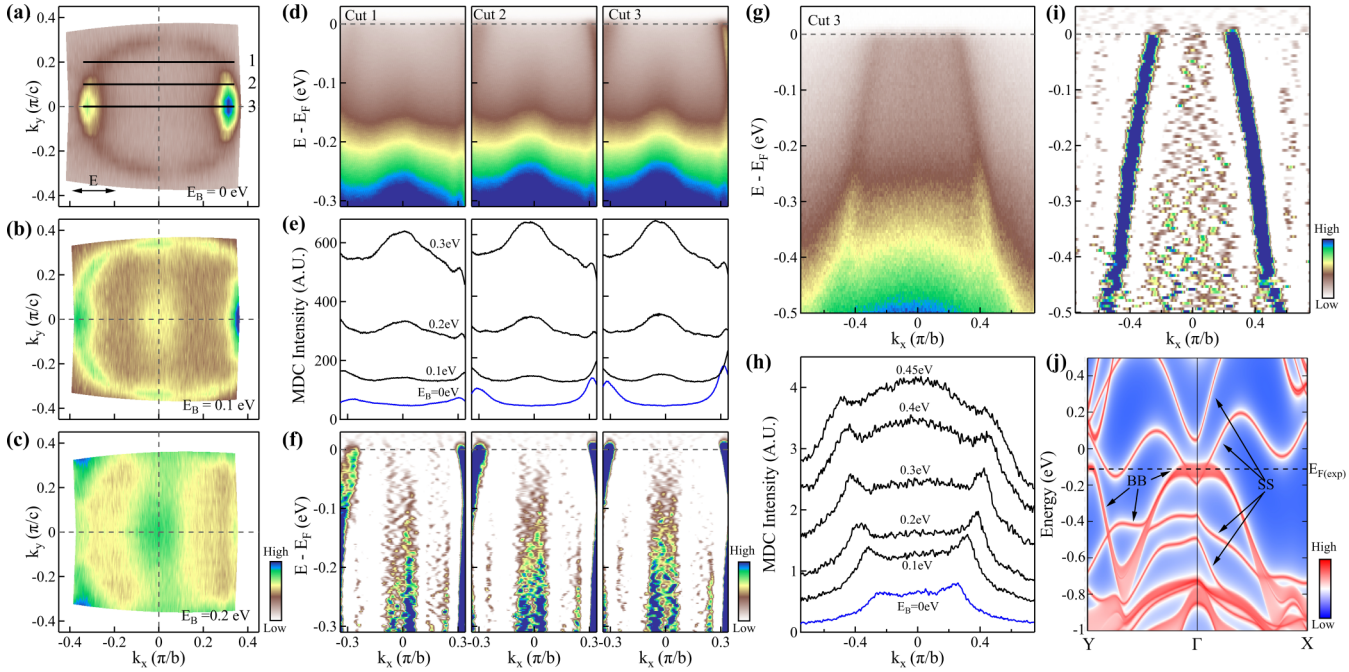

FIG. 5. Detailed electronic structure of $CaMnSb_2$ around the Γ point measured at 30 K. Constant-energy contours around Γ obtained by integrating the photoemission spectral weight over a [−10, 10] meV energy window with respect to (a) 0 eV, (b) 0.1 eV, and (c) 0.2 eV binding energies. The data are the same as in Fig. 4(a) measured with a 6.994 eV laser, and the E vector is along the k_x direction, as marked by the arrow in the inset in (a). (d) Band structure measured along various momentum cuts; the locations of the momentum cuts are marked by black lines in (a). (e) MDCs at the different binding energies from the bands in (d) measured along various momentum cuts. (f) The corresponding second-derivative images with respect to the momentum of the band structures in (d). (g) Band structure measured with a 21.218 eV helium lamp along the horizontal Γ-X direction [the same as cut 3 marked by the black line in (a)]. (h) MDCs at the different binding energies from the band structure in (g). (i) The corresponding second-derivative image with respect to momentum of the band structure in (g). (j) DFT-projected bulk bands and surface bands of the Sb-terminated (100) surface along the Y-Γ-X directions.

surface are allowed for domain A but are fully suppressed for domain B, which is 90° rotated with respect to domain A; the measured Fermi surface mainly comes from one domain, A. By a similar analysis, the rotated pattern in Fig. 4(b) can be understood when the light polarization is 90° rotated because the measured Fermi surface in this case comes mainly from another domain, B.

In addition to the holelike Fermi pocket, we also observed another band around the Γ point, as can be seen in Fig. 4(c). In Fig. 5, we focus on this feature by analyzing the data taken with both the 6.994 eV laser and the 21.218 eV helium lamp. Figures 5(a)–5(c) show Fermi surface and constant-energy contours at different binding energies measured using 6.994 eV photon energy. Three typical bands measured along the momentum cuts parallel to the Γ-X direction are shown in Fig. 5(d). The central band is observed for all three momentum cuts at different k_y. The MDC analyses in Fig. 5(e) indicate that this central band is weak at the Fermi level and low binding energy. It gets stronger with increasing binding energy and becomes dominant at high binding energy. The central band can be more clearly visualized in the second-derivative images in Fig. 5(f); it appears to be composed of two nearly vertical bands on the two sides of the momenta along the Γ-Y line. The persistence of this band for the momentum cuts at different k_y results in a strong intensity patch around the Γ-Y line at a high binding energy, as shown in Fig. 5(c). This band is also observed in the measurements using 21.218 eV helium lamp [Figs. 5(g), 5(h), and 5(i)]. In this case, we find that the signal of the holelike band sits on top of a strong background formed by the electronic states around the Γ point [Fig. 5(h)]. The existence of the band at Γ and along Γ-Y line is clear. But the band structure calculations [Fig. 1(g)] do not reproduce the corresponding band at the Γ point within the 0.5 eV energy range below the Fermi level. In order to find out whether this band stems from surface states, we also calculated the surface states in $CaMnSb_2$, as shown in Fig. 5(j). We find that the new band observed at the Γ point cannot be attributed to the surface states either. The origin of this additional band needs further investigation.

Our present ARPES measurements on $CaMnSb_2$ make it possible to compare it with $SrMnSb_2$ and $BaMnSb_2$ to investigate the effect of replacing the alkali earth metal elements in $AMnSb_2$ (A=Ca, Sr, Ba) in the electronic structures. $BaMnSb_2$ crystalizes in the $I2mm$ space group, and from the ARPES measurement, two small hole pockets near the Y point are observed [59,72]. On the other hand, $CaMnSb_2$ crystalizes in the $Pnma$ space group, and from our ARPES measurements, there is only one hole pocket at the Y point. Therefore, there is a significant difference between $CaMnSb_2$ and $BaMnSb_2$ in both the crystal structure and electronic structure. Although the band structure of $CaMnSb_2$ is similar to $SrMnSb_2$ [71] in some aspects, from our high-resolution

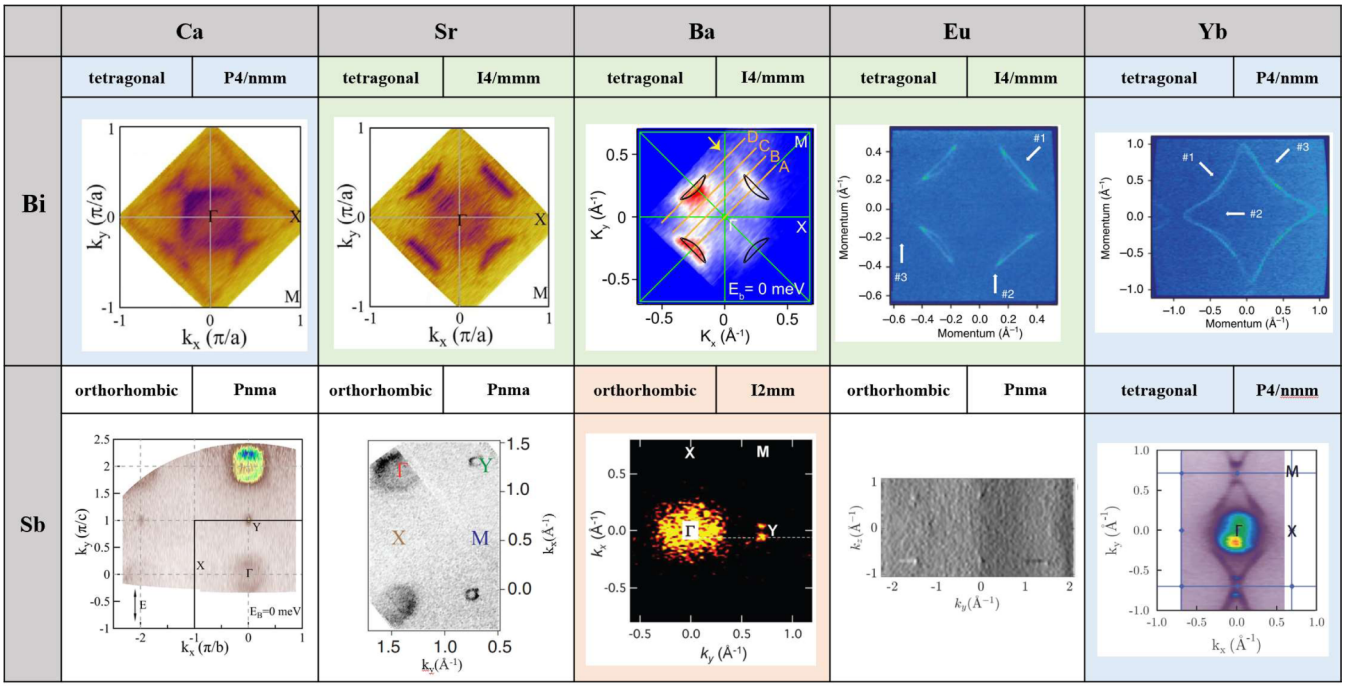

FIG. 6. Summary of crystal structures and electronic structures of $AMnP_2$ (A=Ca, Sr, Ba, Eu, Yb; P=Sb, Bi). Four kinds of crystal structures are identified with $CaMnBi_2$ [50], $YbMnBi_2$ [56], and $YbMnSb_2$ [73] crystalized in the $P4/nmm$ space group; $SrMnBi_2$ [47,50], $BaMnBi_2$ [75], and $EuMnBi_2$ [56] in the $I4/mmm$ space group; $BaMnSb_2$ [59,72] in the $I2mm$ space group; and $CaMnSb_2$, $SrMnSb_2$, [71] and $EuMnSb_2$ [76] in the $Pnma$ space group. The representative measured Fermi surface mapping for each compound is displayed.

ARPES measurements, we have uncovered observations in $CaMnSb_2$ that are distinct from $SrMnSb_2$. First, the strong spectral weight variation along the holelike Fermi surface around Γ in $CaMnSb_2$ is not observed in $SrMnSb_2$ [71]. Second, we revealed an additional band around Γ in $CaMnSb_2$ that is not observed in $SrMnSb_2$ [71]. Third, we find that the tiny hole pocket at the Y point originates from an anisotropic Dirac-like band with the crossing point of the linear bands lying ∼10 meV above the Fermi level in $CaMnSb_2$, while it is ∼200 meV above the Fermi level in $SrMnSb_2$ [71]. This indicates that the Dirac-like band in $CaMnSb_2$ is unique in generating exotic physical properties. In $SrMnSb_2$, the findings of the spectral weight variation and the additional band around Γ in $CaMnSb_2$ were not observed, possibly because the measurement conditions are different. It is interesting to investigate whether, by carrying out high-resolution laser-based ARPES measurements, similar behaviors can be observed in $SrMnSb_2$. On the other hand, the obvious difference in the energy positions of the linear band crossing point at the Y point between $CaMnSb_2$ and $SrMnSb_2$ reflects the intrinsic properties of the measured materials.

It has been found that the electronic structures and topological properties of $AMnP_2$ are intimately connected to their crystal structures. So far four distinct crystal structures have been identified in $AMnP_2$. In Fig. 6, we summarize crystal structures and electronic structures of $AMnP_2$ (A=Ca, Sr, Ba, Eu or Yb; P=Sb or Bi). For $CaMnBi_2$ [50], $YbMnBi_2$, [56] and $YbMnSb_2$ [73] in the $P4/nmm$ space group, the Fermi surface mainly consists of a large diamondlike Fermi surface connecting four equivalent X points in the first Brillouin zone. Dirac cones with a small gap opening at the Dirac point are formed along the diamondlike Fermi surface, with the energy position of the Dirac points varying slightly in momentum space. For $SrMnBi_2$ [47,50,74], $BaMnBi_2$ [75], and $EuMnBi_2$ [56] in the $I4/mmm$ space group, the Fermi surface shows four separated crescent-moon-like segments along the Γ-M direction. In this case, Dirac cones are also formed along a line, but the gap opening at the Dirac point is small along Γ-M and gets much larger along the Γ-X direction. For $BaMnSb_2$ [59,72] in the $I2mm$ space group, its Fermi surface is composed mainly of a large holelike pocket around the Γ point and two Dirac conelike hole pockets around the Y point. For $SrMnSb_2$ [71], $EuMnSb_2$ [76], and $CaMnSb_2$ in the $Pnma$ space group, the Fermi surface consists of a holelike pocket around the Γ point but only one Dirac-cone-like hole pocket at the Y point.

The Fermi surface of $CaMnSb_2$ mainly consists of one hole pocket around the Γ point and one tiny Dirac-cone-like hole pocket at the Y point. We have found that the electronic states along the holelike Fermi surface experience strong scattering because the measured EDCs are broad [Fig. 4(f)]. On the other hand, the electrons on the tiny hole pocket at the Y point experience much less scattering because a coherence peak can be observed [Fig. 3(e)]. Therefore, the tiny hole pocket at the Y point plays a more important role in dictating the physical properties of $CaMnSb_2$. A quantum oscillation measurement detected a Fermi pocket with an area of 0.0008 $Å^{-2}$ [61], which agrees well with the measured area of the tiny hole pocket at Y (∼0.0007 $Å^{-2}$). But another Fermi pocket with an area of 0.0015 $Å^{-2}$ in the quantum oscillation measurement [61] has no clear correspondence in our ARPES measurements. On the other hand, the holelike Fermi

pocket around Γ in our ARPES measurements is not detected in the quantum oscillation measurement [61]. This may be related to the strong electron scattering on this holelike Fermi pocket.

IV. CONCLUSION

In summary, we have carried out detailed high-resolution ARPES measurements and band structure calculations to study the electronic structure of $CaMnSb_2$. The observed Fermi surface mainly consists of one hole pocket around the Γ point and one tiny hole pocket at the Y point. We found strong spectral weight accumulation along the Γ-X direction on the holelike Fermi surface around the Γ point, suggesting strong anisotropy of the density of states along the Fermi surface. The tiny hole pocket at the Y point originates from an anisotropic Dirac-like band with the crossing point of the linear bands lying ∼10 meV above the Fermi level. These observations are in good agreement with the band structure calculations. In addition, we also observed additional features along the Γ-Y line that cannot be accounted for by the band structure calculations. Our results indicate that the Dirac-like structure at the Y point may play an important role in dictating the physical properties of $CaMnSb_2$. They provide important information in the understanding and exploration of novel properties in $CaMnSb_2$ and related materials.

ACKNOWLEDGMENTS

This work is supported by the National Key Research and Development Program of China (Grants No. 2016YFA0300600, No. 2018YFA0305602, No. 2016YFA0300300, and No. 2017YFA0302900), the National Natural Science Foundation of China (Grants No. 11974404, No. 11888101, No. 11922414, and No. 11404175), the Strategic Priority Research Program (B) of the Chinese Academy of Sciences (Grants No. XDB33000000 and No. XDB25000000), the Youth Innovation Promotion Association of CAS (Grant No. 2017013), and the Natural Science Foundation of Henan Province (Grants No. 182300410274 and No. 202300410296). The theoretical calculations were supported by the National Natural Science Foundation of China (Grants No. 11674369, No. 11865019, and No. 11925408), the Beijing Natural Science Foundation (Grant No. Z180008), the Beijing Municipal Science and Technology Commission (Grant No. Z191100007219013), the National Key Research and Development Program of China (Grants No. 2016YFA0300600 and No. 2018YFA0305700), the K. C. Wong Education Foundation (Grant No. GJTD-2018-01).

H.R., L.Z., J. He, and C.S. contributed equally to this work. X.J.Z. and H.R. proposed and designed the research. H.R. and Y.X. carried out the ARPES experiments. L.Z. and H.W. contributed to the band structure calculations. J. He and G.C. prepared the samples; H.R., C.S., J. Huang, C.H., Y.X., Y.C., H.C., C.L., Q.W., L.Z., Z.Z., G.L., Z.X., and X.J.Z. contributed to the development and maintenance of laser-ARPES systems, the data analysis, and the related software development. X.J.Z. and H.R. wrote the paper. All authors participated in discussions and comments on the paper. The authors declare no competing financial interests.

[1] M. Z. Hasan and C. L. Kane, Colloquium: Topological insulators, Rev. Mod. Phys. **82**, 3045 (2010).
[2] X. L. Qi and S. C. Zhang, Topological insulators and superconductors, Rev. Mod. Phys. **83**, 1057 (2011).
[3] A. Bansil, H. Lin and T. Das, Colloquium: Topological band theory, Rev. Mod. Phys. **88**, 021004 (2016).
[4] C. Fang, H. Weng, X. Dai, and Z. Fang, Topological nodal line semimetals, Chin. Phys. B **25**, 117106 (2016).
[5] B. Yan and C. Felser, Topological materials: Weyl semimetals, Annu. Rev. Condens. Matter. Phys. **8**, 337 (2017).
[6] N. P. Armitage, E. J. Mele, and A. Vishwanath, Weyl and Dirac semimetals in three-dimensional solids, Rev. Mod. Phys. **90**, 015001 (2018).
[7] Y. Tokura, K. Yasuda, and A. Tsukazaki, Magnetic topological insulators, Nat. Rev. Phys. **1**, 126 (2019).
[8] C. L. Kane and E. J. Mele, Quantum Spin Hall Effect in Graphene, Phys. Rev. Lett. **95**, 226801 (2005).
[9] C. L. Kane and E. J. Mele, Z_2 Topological Order and the Quantum Spin Hall Effect, Phys. Rev. Lett. **95**, 146802 (2005).
[10] B. A. Bernevig, T. L. Hughes, and S. C. Zhang, Quantum spin Hall effect and topological phase transition in HgTe quantum wells, Science **314**, 1757 (2007).
[11] M. König, S. Wiedmann, C. Brune, A. Roth, H. Buhmann, L. W. Molenkamp, X. L. Qi, and S. C. Zhang, Quantum spin Hall insulator state in HgTe quantum wells, Science **318**, 766 (2007).
[12] L. Fu, C. L. Kane, and E. J. Mele, Topological Insulators in Three Dimensions, Phys. Rev. Lett. **98**, 106803 (2007).
[13] J. E. Moore and L. Balents, Topological invariants of time-reversal-invariant band structures, Phys. Rev. B **75**, 121306(R) (2007).
[14] R. Roy, Topological phases and the quantum spin Hall effect in three dimensions, Phys. Rev. B **79**, 195322 (2009).
[15] D. Hsieh, D. Qian, L. Wray, Y. Xia, Y. S. Hor, R. J. Cava, and M. Z. Hasan, A topological Dirac insulator in a quantum spin Hall, Nature (London) **452**, 970 (2008).
[16] Y. Xia, D. Qian, D. Hsieh, L. Wray, A. Pal, H. Lin, A. Bansil, D. Grauer, Y. S. Hor, R. J. Cava, and M. Z. Hasan, Observation of a large-gap topological-insulator class with a single Dirac cone on the surface, Nat. Phys. **5**, 398 (2009).
[17] Y. L. Chen, J. G. Analytis, J. H. Chu, Z. K. Liu, S. K. Mo, X. L. Qi, H. J. Zhang, D. H. Lu, X. Dai, Z. Fang, S. C. Zhang, I. R. Fisher, Z. Hussain, and Z. X. Shen, Experimental realization of a three-dimensional topological insulator, Bi_2Te_3, Science **325**, 178 (2009).
[18] P. A. M. Dirac, The quantum theory of electron, Proc. R. Soc. London, Ser. A **117**, 610 (1928).
[19] Z. Wang, Y. Sun, X.-Q. Chen, C. Franchini, G. Xu, H. Weng, X. Dai, and Z. Fang, Dirac semimetal and topological phase transitions in A_3Bi (A = Na, K, Pb), Phys. Rev. B **85**, 195320 (2012).

[20] Z. K. Liu, B. Zhou, Y. Zhang, Z. J. Wang, H. M. Weng, D. Prabhakaran, S. K. Mo, Z. X. Shen, Z. Fang, X. Dai, Z. Hussain, and Y. L. Chen, Discovery of a three-dimensional topological Dirac semimetal, Na_3Bi, Science **343**, 864 (2014).

[21] A. Liang *et al.*, Electronic structure, Dirac points and Fermi arc surface states in three-dimensional Dirac semimetal Na_3Bi from angle-resolved photoemission spectroscopy, Chin. Phys. B **25**, 077101 (2016).

[22] Z. K. Liu, J. Jiang, B. Zhou, Z. J. Wang, Y. Zhang, H. M. Weng, D. Prabhakaran, S. K. Mo, H. Peng, P. Dudin, T. Kim, M. Hoesch, Z. Fang, X. Dai, Z. X. Shen, D. L. Feng, Z. Hussain and Y. L. Chen, A stable three-dimensional topological Dirac semimetal Cd_3As_2, Nat. Mater. **13**, 677 (2014).

[23] M. Neupane, S. Y. Xu, R. Sankar, N. Alidoust, G. Bian, C. Liu, I. Belopolski, T. R. Chang, H. T. Jeng, H. Lin, A. Bansil, F. Chou, and M. Z. Hasan, Observation of a three-dimensional topological Dirac semimetal phase in high-mobility Cd_3As_2, Nat. Commun. **5**, 3786 (2014).

[24] H. Yi *et al.*, Evidence of topological surface state in three-dimensional Dirac semimetal Cd_3As_2, Sci. Rep. **4**, 6106 (2014).

[25] X. Wan, A. M. Turner, A. Vishwanath, and S. Y. Savrasov, Topological semimetal and Fermi-arc surface states in the electronic structure of pyrochlore iridates, Phys. Rev. B **83**, 205101 (2011).

[26] S. M. Huang, S. Y. Xu, I. Belopolski, C. C. Lee, G. Chang, B. Wang, N. Alidoust, G. Bian, M. Neupane, C. Zhang, S. Jia, A. Bansil, H. Lin, and M. Z. Hasan, A Weyl fermion semimetal with surface Fermi arcs in the transition metal monopnictide TaAs class, Nat. Commun. **6**, 7373 (2015).

[27] H. Weng, C. Fang, Z. Fang, B. A. Bernevig, and X. Dai, Weyl Semimetal Phase in Noncentrosymmetric Transition-Metal Monophosphides, Phys. Rev. X **5**, 011029 (2015).

[28] S. Y. Xu *et al.*, Discovery of a Weyl fermion semimetal and topological Fermi arcs, Science **349**, 613 (2015).

[29] L. X. Yang, Z. K. Liu, Y. Sun, H. Peng, H. F. Yang, T. Zhang, B. Zhou, Y. Zhang, Y. F. Guo, M. Rahn, D. Prabhakaran, Z. Hussain, S. K. Mo, C. Felser, B. Yan, and Y. L. Chen, Weyl semimetal phase in the non-centrosymmetric compound TaAs, Nat. Phys. **11**, 728 (2015).

[30] B. Q. Lv, H. M. Weng, B. B. Fu, X. P. Wang, H. Miao, J. Ma, P. Richard, X. C. Huang, L. X. Zhao, G. F. Chen, Z. Fang, X. Dai, T. Qian, and H. Ding, Experimental Discovery of Weyl Semimetal TaAs, Phys. Rev. X **5**, 031013 (2015).

[31] A. A. Burkov, M. D. Hook, and L. Balents, Topological nodal semimetals, Phys. Rev. B **84**, 235126 (2011).

[32] L. M. Schoop, M. N. Ali, C. Strasser, A. Topp, A. Varykhalov, D. Marchenko, V. Duppel, S. S. Parkin, B. V. Lotsch, and C. R. Ast, Dirac cone protected by non-symmorphic symmetry and three-dimensional Dirac line node in ZrSiS, Nat. Commun. **7**, 11696 (2016).

[33] M. Neupane, I. Belopolski, M. M. Hosen, D. S. Sanchez, R. Sankar, M. Szlawska, S.-Y. Xu, K. Dimitri, N. Dhakal, P. Maldonado, P. M. Oppeneer, D. Kaczorowski, F. Chou, M. Z. Hasan, and T. Durakiewicz, Observation of topological nodal fermion semimetal phase in ZrSiS, Phys. Rev. B **93**, 201104(R) (2016).

[34] Y. Wang *et al.*, Spectroscopic evidence for the realization of a genuine topological nodal-line semimetal in LaSbTe, Phys. Rev. B **103**, 125131 (2021).

[35] T. O. Wehling, A. M. Black-Schaffer, and A. V. Balatsky, Dirac materials, Adv. Phys. **63**, 1 (2014).

[36] H. D. Song, D. Sheng, A. Q. Wang, J. G. Li, D. P. Yu, and Z. M. Liao, Topological transport in Dirac electronic systems: A concise review, Chin. Phys. B **26**, 037301 (2017).

[37] H. Wang and J. Wang, Electron transport in Dirac and Weyl semimetals, Chin. Phys. B **27**, 107402 (2018).

[38] K. S. Novoselov, A. K. Geim, S. V. Morozov, D. Jiang, M. I. Katsnelson, I. V. Grigorieva, S. V. Dubonos, and A. A. Firsov, Two dimensional gas of massless Dirac fermions in graphene, Nature (London) **438**, 197 (2005).

[39] Y. Zhang, Y. W. Tan, H. L. Stormer, and P. Kim, Experimental observation of the quantum Hall effect and Berry's phase in graphene, Nature (London) **438**, 201 (2005).

[40] S. A. Parameswaran, T. Grover, D. A. Abanin, D. A. Pesin, and A. Vishwanath, Probing the Chiral Anomaly with Nonlocal Transport in Three-Dimensional Topological Semimetals, Phys. Rev. X **4**, 031035 (2014).

[41] J. Xiong, S. K. Kushwaha, T. Liang, J. W. Krizan, M. Hirschberger, W. Wang, R. J. Cava, and N. P. Ong, Evidence for the chiral anomaly in the Dirac semimetal Na_3Bi, Science **350**, 413 (2015).

[42] Z. Wang, H. Weng, Q. Wu, X. Dai, and Z. Fang, Three-dimensional Dirac semimetal and quantum transport in Cd_3As_2, Phys. Rev. B **88**, 125427 (2013).

[43] T. Liang, Q. Gibson, M. N. Ali, M. Liu, R. J. Cava, and N. P. Ong, Ultrahigh mobility and giant magnetoresistance in the Dirac semimetal Cd_3As_2, Nat. Mater. **14**, 280 (2015).

[44] J. Feng, Y. Pang, D. Wu, Z. Wang, H. Weng, J. Li, X. Dai, Z. Fang, Y. Shi, and L. Lu, Large linear magnetoresistance in Dirac semimetal Cd_3As_2 with Fermi surfaces close to the Dirac points, Phys. Rev. B **92**, 081306(R) (2015).

[45] Y. Zhao, H. Liu, C. Zhang, H. Wang, J. Wang, Z. Lin, Y. Xing, H. Lu, J. Liu, Y. Wang, S. M. Brombosz, Z. Xiao, S. Jia, X. C. Xie, and J. Wang, Anisotropic Fermi Surface and Quantum Limit Transport in High Mobility Three-Dimensional Dirac Semimetal Cd_3As_2, Phys. Rev. X **5**, 031037 (2015).

[46] L. X. Wang, C. Z. Li, D. P. Yu, and Z. M. Liao, Aharonov-Bohm oscillations in Dirac semimetal Cd_3As_2 nanowires, Nat. Commun. **7**, 10769 (2016).

[47] J. Park, G. Lee, F. Wolff-Fabris, Y. Y. Koh, M. J. Eom, Y. K. Kim, M. A. Farhan, Y. J. Jo, C. Kim, J. H. Shim, and J. S. Kim, Anisotropic Dirac Fermions in a Bi Square Net of $SrMnBi_2$, Phys. Rev. Lett. **107**, 126402 (2011).

[48] J. K. Wang, L. L. Zhao, Q. Yin, G. Kotliar, M. S. Kim, M. C. Aronson, and E. Morosan, Layered transition-metal pnictide $SrMnBi_2$ with metallic blocking layer, Phys. Rev. B **84**, 064428 (2011).

[49] Y. J. Jo, J. Park, G. Lee, M. J. Eom, E. S. Choi, J. H. Shim, W. Kang, and J. S. Kim, Valley-Polarized Interlayer Conduction of Anisotropic Dirac Fermions in $SrMnBi_2$, Phys. Rev. Lett. **113**, 156602 (2014).

[50] Y. Feng *et al.*, Strong anisotropy of Dirac cones in $SrMnBi_2$ and $CaMnBi_2$ revealed by angle-resolved photoemission spectroscopy, Sci. Rep. **4**, 5385 (2014).

[51] J. Y. Liu, J. Hu, Q. Zhang, D. Graf, H. B. Cao, S. M. A. Radmanesh, D. J. Adams, Y. L. Zhu, G. F. Cheng, X. Liu, W. A. Phelan, J. Wei, M. Jaime, F. Balakirev, D. A. Tennant, J. F. Ditusa, I. Chiorescu, L. Spinu, and Z. Q. Mao, A magnetic

topological semimetal $Sr_{1-y}Mn_{1-z}Sb_2$ (y, z <0.1), Nat. Mater. **16**, 905 (2017).

[52] H. Masuda, H. Sakai, M. Tokunaga, Y. Yamasaki, A. Miyake, J. Shiogai, S. Nakamura, S. Awaji, A. Tsukazaki, H. Nakao, Y. Murakami, T. H. Arima, Y. Tokura, and S. Ishiwata, Quantum Hall effect in a bulk antiferromagnet $EuMnBi_2$ with magnetically confined two-dimensional Dirac fermions, Sci. Adv. **2**, e1501117 (2016).

[53] A. Zhang, C. Liu, C. Yi, G. Zhao, T. L. Xia, J. Ji, Y. Shi, R. Yu, X. Wang, C. Chen, and Q. Zhang, Interplay of Dirac electrons and magnetism in $CaMnBi_2$ and $SrMnBi_2$, Nat. Commun. **7**, 13833 (2016).

[54] J. Y. Liu, J. Hu, D. Graf, T. Zou, M. Zhu, Y. Shi, S. Che, S. M. A. Radmanesh, C. N. Lau, L. Spinu, H. B. Cao, X. Ke, and Z. Q. Mao, Unusual interlayer quantum transport behavior caused by the zeroth Landau level in $YbMnBi_2$, Nat. Commun. **8**, 646 (2017).

[55] Y. Shiomi, H. Watanabe, H. Masuda, H. Takahashi, Y. Yanase, and S. Ishiwata, Observation of a Magnetopiezoelectric Effect in the Antiferromagnetic Metal $EuMnBi_2$, Phys. Rev. Lett. **122**, 127207 (2019).

[56] S. Borisenko, D. Evtushinsky, Q. Gibson, A. Yaresko, K. Koepernik, T. Kim, M. Ali, J. Van Den Brink, M. Hoesch, A. Fedorov, E. Haubold, Y. Kushnirenko, I. Soldatov, R. Schafer, and R. J. Cava, Time-reversal symmetry breaking type-II Weyl state in $YbMnBi_2$, Nat. Commun. **10**, 3424 (2019).

[57] R. Yang, M. Corasaniti, C. C. Le, Z. Y. Liao, A. F. Wang, Q. Du, C. Petrovic, X. G. Qiu, J. P. Hu, and L. Degiorgi, Spin-Canting-Induced Band Reconstruction in the Dirac Material $Ca_{1-x}Na_xMnBi_2$, Phys. Rev. Lett. **124**, 137201 (2020).

[58] J. Yu and C. X. Liu, Piezoelectricity and topological quantum phase transitions in two-dimensional spin-orbit coupled crystals with time-reversal symmetry, Nat. Commun. **11**, 2290 (2020).

[59] J. Y. Liu *et al.*, Spin-valley locking, bulk quantum Hall effect and chiral surface state in a noncentrosymmetric Dirac semimetal $BaMnSb_2$, arXiv:1907.06318.

[60] G. Lee, M. A. Farhan, J. S. Kim, and J. H. Shim, Anisotropic Dirac electronic structures of $AMnBi_2$ (A = Sr, Ca), Phys. Rev. B **87**, 245104 (2013).

[61] J. B. He, Y. Fu, L. X. Zhao, H. Liang, D. Chen, Y. M. Leng, X. M. Wang, J. Li, S. Zhang, M. Q. Xue, C. H. Li, P. Zhang, Z. A. Ren, and G. F. Chen, Quasi-two-dimensional massless Dirac fermions in $CaMnSb_2$, Phys. Rev. B **95**, 045128 (2017).

[62] Z. Qiu, C. Le, Y. Dai, B. Xu, J. B. He, R. Yang, G. Chen, J. Hu, and X. Qiu, Infrared spectroscopic studies of the topological properties in $CaMnSb_2$, Phys. Rev. B **98**, 115151 (2018).

[63] G. Liu, G. Wang, Y. Zhu, H. Zhang, G. Zhang, X. Wang, Y. Zhou, W. Zhang, H. Liu, L. Zhao, J. Meng, X. Dong, C. Chen, Z. Xu, and X. J. Zhou, Development of a vacuum ultraviolet laser-based angle-resolved photoemission system with a super-high energy resolution better than 1 meV, Rev. Sci. Instrum. **79**, 023105 (2008).

[64] X. Zhou, S. He, G. Liu, L. Zhao, L. Yu, and W. Zhang, New developments in laser-based photoemission spectroscopy and its scientific applications: A key issues review, Rep. Prog. Phys. **81**, 062101 (2018).

[65] G. Kresse and J. Furthmuller, Efficient iterative schemes for ab initio total-energy calculations using a plane-wave basis set, Phys. Rev. B **54**, 11169 (1996).

[66] J. P. Perdew, K. Burke, and M. Ernzerhof, Generalized Gradient Approximation Made Simple, Phys. Rev. Lett. **77**, 3865 (1996).

[67] A. D. Becke and E. R. Johnson, A simple effective potential for exchange, J. Chem. Phys. **124**, 221101 (2006).

[68] F. Tran and P. Blaha, Accurate Band Gaps of Semiconductors and Insulators with a Semilocal Exchange-Correlation Potential, Phys. Rev. Lett. **102**, 226401 (2009).

[69] A. A. Mostofi, J. R. Yates, G. Pizzi, Y.-S. Lee, I. Souza, D. Vanderbilt, and N. Marzari, An updated version of wannier 90: A tool for obtaining maximally-localised Wannier functions, Comput. Phys. Commun. **185**, 2309 (2014).

[70] Q. Wu, S. Zhang, H.-F. Song, M. Troyer, and A. A. Soluyanov, WannierTools: An open-source software package for novel topological materials, Comput. Phys. Commun. **224**, 405 (2018).

[71] S. V. Ramankutty, J. Henke, A. Schiphorst, R. Nutakki, S. Bron, G. Araizi-Kanoutas, S. Mishra, L. Li, Y. Huang, T. Kim, M. Hoesch, C. Schlueter, T.-L. Lee, A. De Visser, Z. Zhong, J. Van Wezel, E. Van Heumen, and M. Golden, Electronic structure of the candidate 2D Dirac semimetal $SrMnSb_2$: A combined experimental and theoretical study, SciPost Phys. **4**, 010 (2018).

[72] H. Sakai, H. Fujimura, S. Sakuragi, M. Ochi, R. Kurihara, A. Miyake, M. Tokunaga, T. Kojima, D. Hashizume, T. Muro, K. Kuroda, T. Kondo, T. Kida, M. Hagiwara, K. Kuroki, M. Kondo, K. Tsuruda, H. Murakawa, and N. Hanasaki, Bulk quantum Hall effect of spin-valley coupled Dirac fermions in the polar antiferromagnet $BaMnSb_2$, Phys. Rev. B **101**, 081104(R) (2020).

[73] R. Kealhofer, S. Jang, S. M. Griffin, C. John, K. A. Benavides, S. Doyle, T. Helm, P. J. W. Moll, J. B. Neaton, J. Y. Chan, J. D. Denlinger, and J. G. Analytis, Observation of a two-dimensional Fermi surface and Dirac dispersion in $YbMnSb_2$, Phys. Rev. B **97**, 045109 (2018).

[74] L. L. Jia, Z. H. Liu, Y. P. Cai, T. Qian, X. P. Wang, H. Miao, P. Richard, Y. G. Zhao, Y. Li, D. M. Wang, J. B. He, M. Shi, G. F. Chen, H. Ding, and S. C. Wang, Observation of well-defined quasiparticles at a wide energy range in a quasi-two-dimensional system, Phys. Rev. B **90**, 035133 (2014).

[75] H. Ryu, S. Y. Park, L. Li, W. Ren, J. B. Neaton, C. Petrovic, C. Hwang, and S. K. Mo, Anisotropic Dirac fermions in $BaMnBi_2$ and $BaZnBi_2$, Sci. Rep. **8**, 15322 (2018).

[76] J. R. Soh, P. Manuel, N. M. B. Schröter, C. J. Yi, F. Orlandi, Y. G. Shi, D. Prabhakaran, and A. T. Boothroyd, Magnetic and electronic structure of Dirac semimetal candidate $EuMnSb_2$, Phys. Rev. B **100**, 174406 (2019).